Optical study of beyond EUV mask and mirrors

Naoki Hayase,[a] Shinji Yamakawa,[a] Tetsuo Harada[a]

[a] Center for EUV lithography, LASTI, University of Hyogo, NewSUBARU synchrotron radiation facility, Ako-gun Kamigori Kouto 1-1-2, Hyogo 678-1205, Japan

Abstract: Beyond EUV (BEUV) lithography at around 6.6 nm wavelength suffers from the small refractive-index contrast and requires around 200 pairs of multilayer (ML) mirrors. The large number of ML interfaces amplifies scattered light arising from surface roughness, and a greater effective reflection plane depth (Z_{eff}) in ML drives mask 3D effect (M3D) in photomasks. **Background:** The problems originate from the same low-contrast constraint, but our previous study neither linked reactive surface growth to the former, nor quantified the nitride absorber against M3D in the latter. **Aim**: We investigate nitride-based BEUV optics to control kinetic roughness during gas-reactive deposition and identify a promising BEUV mask to improve optical performance. **Approach**: Reactive nitride growth is described by a finite-mobility solid-on-solid model in which chemisorbed nitrogen coverage governed by the Langmuir-Hinshelwood kinetics modifies the Ehrlich-Schwoebel (ES) and adatom diffusion barriers. Furthermore, we investigate TaN- and CrN-based BEUV absorbers and their dependences on reflectivity, phase difference, and aerial images. **Results**: Assuming coverage-dependent barriers, the model predicts that roughness decreases with increasing nitrogen chemisorption coverage. As nitride-based components, CrN gives 17.1 % at 62.6 nm thickness with 135° phase shifting, and Mo_2N/B ML has larger Z_{eff} of around 70 nm, which is greater than Mo/Si ML for EUV lithography. **Conclusions**: Nitride interface kinetics provides a route to roughness control for MLs and photomasks. CrN-based Att-PSMs are candidates for high-NA BEUV lithography, considering 0.55 NA with 4x/8x demagnification at an angle of incidence of around 6°.

Keywords: beyond EUV; multilayer; photomask; absorber; optical scattering; deposition; phase shift.

E-mail: hayase@lasti.u-hyogo.ac.jp

1 Introduction

Beyond EUV (BEUV) lithography at around 6.6 nm wavelength has been developed for the further downscaling of semiconductor devices [1,2]. BEUV optics require high-reflectance, high-durability multilayer (ML) mirrors for the design of exposure tools and photomasks. Surface roughness on mirrors causes a decrease in reflectivity with optical scattering. Minimization of surface roughness is necessary to reduce false defect detections in a mask inspection process and improve lithographic patterning [3].

The physical vapor deposition (PVD) process for MLs generally has two approaches: ion beam deposition (IBD) and magnetron sputtering (MS). The roughness of ML deposited by MS is greater than that of IBD, but MS is superior to IBD in terms of throughput for ML deposition in previous works [4,5]. Given an understanding of the deposition mechanism for roughness control, MS is expected to be a primary method for improving the productivity of mirrors and photomasks.

Table 1 shows the performance of EUV, BEUV, and Blue-X lithography, assuming the Rayleigh coefficients are 0.33 and 1.0 for half-pitch (HP) resolution and depth-of-focus (DOF). After 0.75 NA EUV lithography, 0.55 NA BEUV is a candidate for 4 nm HP. In addition, a patterning error of reflection shadowing known as the mask 3D effect (M3D) is a concern, which originates from absorber thickness and effective reflection plane depth (Z_{eff}) of MLs [6]. BEUV ML exhibits a deeper Z_{eff} owing to the smaller difference of refractive index than EUV Mo/Si MLs, resulting in severe M3D and critical dimension (CD) variation at near-normal angles of incidence (AOI) [1]. Photomasks are mainly categorized into binary masks and attenuated phase shift masks (Att-PSMs) [7]. Binary masks rely on the extinction coefficient of materials to reduce reflectivity from ML. BEUV binary absorbers are predicted to require greater thickness than EUV masks, which amplifies M3D-induced CD errors and limits lithographic scalability. In contrast, Att-PSMs exploit controlled phase modulation and partial reflectivity to enhance image contrast. Att-PSMs are expected to allow thinner absorber designs compared with binary masks, by selecting suitable materials.

In this paper, we investigate a surface growth model of nitrogen gas reactive deposition in masks and mirrors for minimizing roughness. Furthermore, we propose a nitride-based Att-PSM structure for suppressing the M3D effect and identify the allowable NA and demagnification (DM) of exposures for high-NA BEUV lithography.

Table 1. Comparison of EUV, BEUV, and Blue-X lithography performance.

Title	Wavelength	NA	Resolution (HP)	DOF	Photomask
EUV	13.5 nm	0.33	13.5 nm	124.0 nm	Binary, Att-PSM
		0.55	8.1 nm	44.6 nm	Att-PSM
		0.75	5.9 nm	24.0 nm	
BEUV	6.6 nm	0.55	4.0 nm	21.8 nm	Undefined
		0.75	2.9 nm	11.7 nm	
Blue-X	3.1 nm	0.27	3.8 nm	42.5 nm	

2 Multilayer mirror

2.1 Surface Scattering

Surface roughness causes diffuse scattering, and total integrated scatter (TIS) represents the fraction of the total scatter and the specular reflection with AOI (θ_i) as given in Eq. (1) [8,9].

$$\mathrm{TIS}_N = 1 - \prod_{k=1}^{N} \exp\left[-\left(\frac{4\pi\sigma\cos\theta_i}{\lambda}\right)^2\right]_k \quad (1)$$

Fig. 1 shows the dependence of TIS on wavelength with the number of reflections, assuming the roughness from 0.1 nm to 0.4 nm with an AOI of 6°. At 6.60 nm wavelength with σ = 0.1 nm, the TIS is 22.2 % after seven reflections, approximately 3.8 times that at 13.50 nm. The TIS is 98.2 % after seven reflections with σ = 0.4 nm, so that, surface roughness in BEUV mirrors is required to be under 0.4 nm, considering near-normal AOI mirrors. At 3.13 nm wavelength, the TIS is 67.2 % at 0.1 nm and 98.8 % at 0.2 nm after seven reflections, and 47.1 % with σ = 0.1 nm and 92.2 % with σ = 0.2 nm even in four reflections, requiring roughness to be under 0.2 nm.

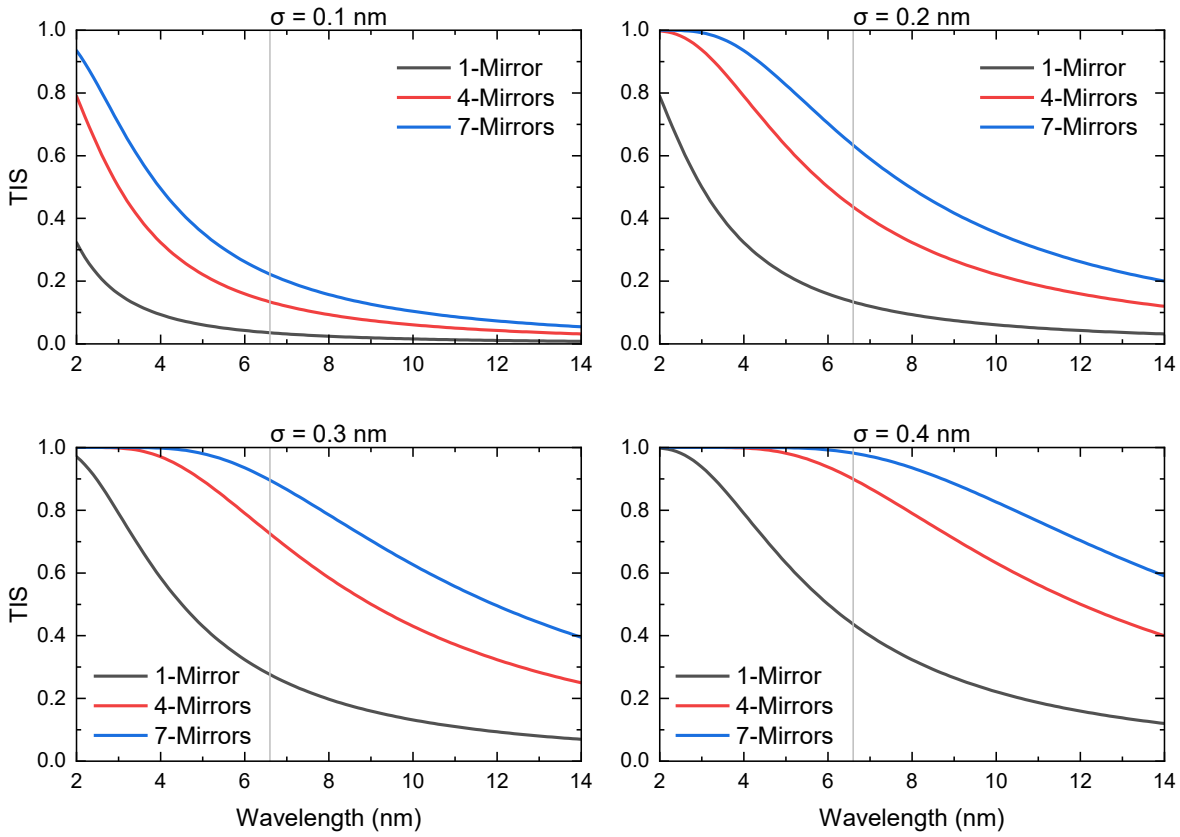

Fig. 1 Dependence of TIS on wavelength with the number of mirrors, assuming the roughness from 0.1 nm to 0.4 nm with AOI of 6°. The grey lines point to 6.6 nm wavelength.

Fig. 2-(a) shows the simulation of normalized reflectivity versus the roughness scaling factor σ/λ where Mo/Si = 2.93 nm/4.03 nm of 40 pairs at 13.50 nm, Mo_2N/B = 1.30/2.00 nm of 200 pairs at 6.60 nm, and Cr/Sc = 0.667 nm/0.90 nm of 500 pairs at 3.13 nm, based on the Parratt model including roughness [10,11]. The normalized reflectance is reduced to half when $\sigma/\lambda = 0.05$ at 3.13 nm, $\sigma/\lambda = 0.10$ at 6.60 nm, and $\sigma/\lambda = 0.24$ at 13.50 nm. This indicates that the allowable roughness is approximately 4.9 times (6.60 nm) and 20.7 times (3.13 nm) smaller than EUV ML. Fig. 2-(b) shows the background level (BGL) as the scattered light intensity, which is defined as the product of reflectance and TIS at 13.50 nm, 6.60 nm, and 3.13 nm. The BGL is suppressed at shorter wavelengths, but the peak positions shift to smaller σ/λ due to the reflectance loss.

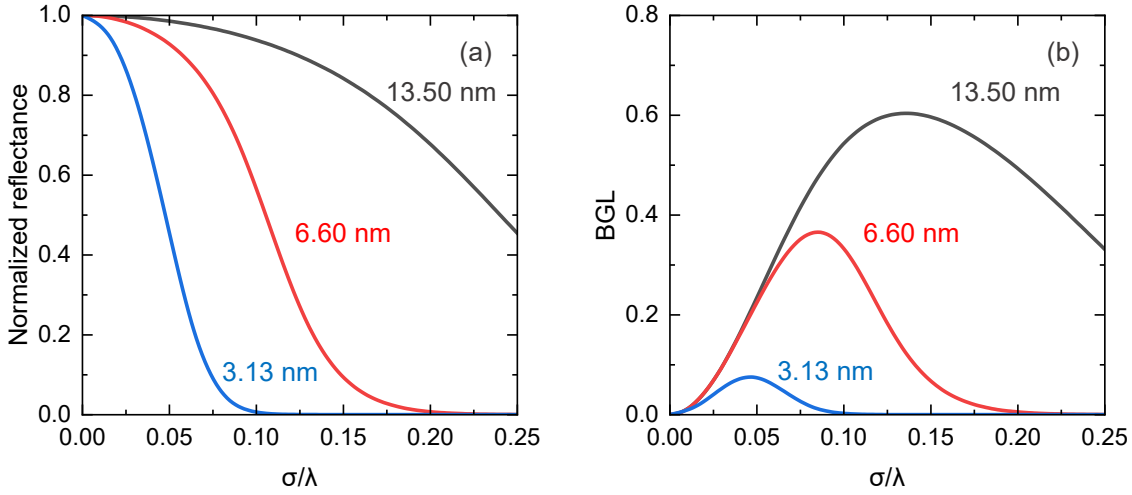

Fig. 2 (a) Normalized reflectivity versus roughness scaling factor at 13.50, 6.60, and 3.13 nm, the AOIs are 6°, (b) Dependence of BGL on roughness scaling factor at 13.50, 6.60, and 3.13 nm.

2.2 Surface growth

We investigate reactive PVD nitride growth as a route to minimizing surface roughness, and the nitrogen coverage denotes the fraction of growth sites chemically bonded as chemisorption. Thin film growth has been reported to belong to the Kardar-Parisi-Zhang (KPZ) universality class, and the 1 dimensional (1D) KPZ equation is used to describe surface growth by Eq. (2) [12,13].

$$\frac{\partial h(x,t)}{\partial t} = \nu\nabla^2 h + \frac{\Lambda}{2}(\nabla h)^2 + \eta(x,t) \quad (2)$$

where ν is a surface relaxation coefficient, Λ is a strength of nonlinear lateral growth term, and $\eta(x,t)$ is a zero-mean white Gaussian noise of intensity. The nonlinear term is discretized using

the Lam-Shin form in Eq. (3), and the equation is integrated by a semi-implicit Fourier method [14].

$$(\nabla h)_i^2 \rightarrow \frac{(s^+)^2 + (s^-)^2 + s^+ s^-}{3\Delta x^2} \tag{3}$$

where $s^+ = h_{i+1} - h_i$, $s^- = h_i - h_{i-1}$ are the local slopes on the 1D chain. Complementing the continuum description with a nanoscale picture, we employ the restricted solid-on-solid (RSOS) model [15,16]. The surface is represented by integer heights h_i subject to the constraint as Eq. (4).

$$|h_{i+1} - h_i| \leq N \tag{4}$$

A site is chosen at random ($P = 1/L$ where L is the number of sites) and a unit deposition $h_i \rightarrow h_i + 1$ is accepted when the constraint of Eq. (4) remains satisfied. Varying the constraint from $N = 1$ to 3 changes the allowed step height but preserves the restricted solid-on-solid (RSOS) character of the surface. We further introduce a finite-mobility SOS model with the Ehrlich-Schwoebel (ES) barrier, that the KPZ and RSOS descriptions leave unspecified as Eq. (5) [17,18].

$$P_{acc} = \begin{cases} 0 & (\Delta h > 0) \\ 1 & (\Delta h = 0) \\ 1 - P_{ES} & (\Delta h < 0) \end{cases} \tag{5}$$

where P_{acc} is the acceptance probability for an attempted hop from site i to a neighboring site j, P_{ES} is the ES reflection probability that interpolates between smooth ($P_{ES} = 0$) and rough ($P_{ES} = 1.0$) growth kinetics, $\Delta h = h_j - h_i$. The growth mode shifts from EW-type smooth growth to KPZ-type, and to the ES-type growth. This reflection encodes the extra barrier for descending a step edge. The diffusion length is limited by a finite mobility q_0, after each hop the walk terminates with probability $1 - q_0$, so that the mean number of hops per atom is $\langle n_{hop} \rangle = 1/(1 - q_0)$. To quantify the roughening of every model on a common footing, we use the surface width (root-mean-square roughness) $W(L,t)$, defined as Eq. (6).

$$W(L,t) = \langle \frac{1}{L} \sum_i (h_i - \langle h \rangle)^2 \rangle^{\frac{1}{2}} \tag{6}$$

In the Family-Vicsek picture, $W(L,t)$ grows as a power law of time before saturation and saturates with system size as Eq. (7) [19].

$$W(L,t) \sim t^{\beta} \ (t \ll t_{sat}), W_{sat} \sim L^{\alpha} \tag{7}$$

where β is the growth exponent as a diagnostic of the scaling behavior, α is the roughness exponent, and $z = \alpha/\beta$ is the dynamic exponent. The 1+1D Edwards-Wilkinson (EW) equation gives β = 1/4 and the KPZ equation gives β = 1/3 [20,21].

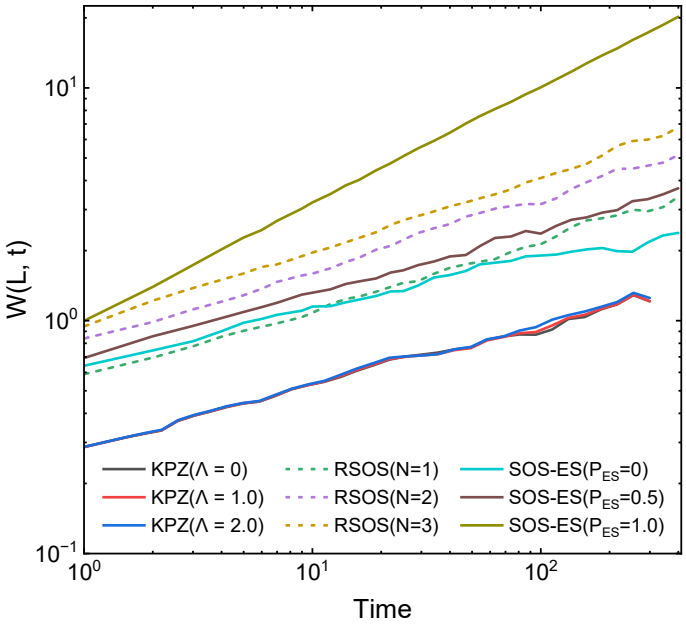

Fig. 3 Simulated kinetic roughening in 1+1D by the KPZ, the RSOS, and the finite-mobility SOS/ES models. The parameters are L = 512, ν = 1.0, Δt = 0.05 for the KPZ, RSOS, and q_0 = 0.9 for the SOS/ES.

Fig. 3 shows the time evolution of the surface width $W(t)$ as simulated roughness by the three models. In the KPZ model, Λ = 0 gives the EW limit, while Λ > 0 approaches 1+1D KPZ value β = 1/3 with finite-time crossover effects remaining. The RSOS model with N = 1, 2, and 3 also yield near β = 1/3 (β changes from 0.30 to 0.33), so they do not provide a direct kinetic parameter for surface smoothing. In contrast, the finite-mobility SOS/ES models change β rising from about 0.2 at P_{ES} = 0 to 0.5 at P_{ES} = 1.0. The value at $P_{ES}(\theta)$ = 1.0 is the effective slope of ES growth, and $P_{ES}(\theta)$ = 0 is the smooth limit.

Chemisorption is assumed to act as a surfactant that lowers both kinetic barriers as the coverage increases: $E_{ES}(\theta) = E_{ES,0}(1-\theta)$ and $E_{diff}(\theta) = E_{diff,0}(1-c_d\theta)$, so that $E_{diff}(\theta)$ sets the surface diffusivity in the case of nitridation as Eq. (8) [22,23].

$$D_s(\theta_N) = D_0 \exp\left[-E_{diff}(\theta_N)/k_B T\right] \tag{8}$$

where θ_N is nitrogen coverage, $E_{ES,0}$ and $E_{diff,0}$ are the initial barriers, $c_d \leq 1$ scales the diffusion-barrier reduction, D_0 is the initial diffusivity. Chemisorption lowers barriers with coverage increase, and mean hops per adatom $\langle n_{hop}\rangle = D_s(\theta_N)\langle t\rangle/a^2$where a^2 is a lattice size, increases with $P_{ES}(\theta)$ decrease. Increasing θ_N lowers E_{ES} and suppresses the ES current that keeps $\nu < 0$ [24]. A reactive interface approaches the EW growth while retaining the Mullins diffusion term of Eq. (9) [25].

$$\frac{\partial h(x,t)}{\partial t} = \nu\nabla^2 h - \kappa_M \nabla^4 h + \eta(x,t) \tag{9}$$

where κ_M is the Mullins surface-diffusion coefficient given by Eq. (10).

$$\kappa_M = \frac{D_s \gamma_s \Omega^2 n_s}{k_B T} \tag{10}$$

where D_s is the surface diffusivity, γ_s is the surface free energy, Ω is the atomic volume, and n_s is the areal density of mobile adatoms. A height mode of wavenumber k decays at $\nu k^2 + \kappa_M k^4$, γ_s enters only through κ_M and rescales the crossover $(\nu/\kappa_M)^{1/2}$ without changing the sign of ν. Therefore, the smoothing is kinetic rather than thermodynamic in origin [24,26,27], and nitrogen coverage follows from the balance between dissociative supply, associative desorption, and surface reaction given by the Langmuir-Hinshelwood (LH) kinetics as Eq. (11) [22].

$$\frac{d\theta_N}{dt} = 2k_a p_N (1-\theta_N)^2 - 2k_d {\theta_N}^2 - k_r \theta_M \theta_N \tag{11}$$

where k_a, k_d, and k_r are the adsorption, desorption, and reaction rate constants, p_N is the nitrogen partial pressure, and θ_M is the coverage of mobile metal adatoms.

Fig. 4 shows the relationship between roughness and nitrogen coverage in 2+1D for assuming single layer thicknesses of 1, 10, and 100 nm with a = 0.25 nm for $W(L,t)$. β drops from the ES value toward the 2+1D KPZ value β ≈ 0.24, with the EW limit being logarithmic. Over the simulated range θ_N ≈ 0.066-0.573, total roughness decreases monotonically. The low-to-high coverage reductions are 37.8 %, 59.9 %, and 69.6 % for 1, 10, and 100 nm.

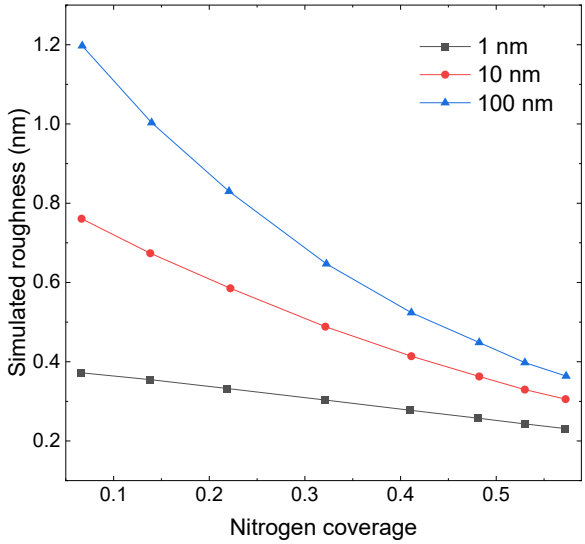

Fig. 4 Simulated relationship between roughness and chemisorption coverage in 2+1D, assuming single layer thickness of 1 nm, 10 nm, and 100 nm thickness. The parameters are L = 256, a = 0.25 nm for $W(L,t)$.

3 Photomask

3.1 Optical constants

Fig. 5 shows the simulated optical constants at 6.60 nm wavelength based on Eqs. (12) and (13), using data from the CXRO database [28,29].

$$n = 1 - \frac{2\pi r_e \rho N_A}{k^2} \frac{\sum_j x_j f_{1j}}{\sum_j x_j A_r(E)} \tag{12}$$

$$\kappa = \frac{2\pi r_e \rho N_A}{k^2} \frac{\sum_j x_j f_{2j}}{\sum_j x_j A_r(E)} \tag{13}$$

where k is wavenumber vector, $r_e = 2.818\times10^{-15}$ m is the classical electron radius, $N_A = 6.022\times10^{23}$ mol^{-1} is the Avogadro number, ρ is the density, $A_r(E)$ is the atomic weight, f_{1j} and f_{2j} are the real and the imaginary parts of the atomic scattering factors, respectively. The density of the compound materials used for the calculation is referenced in Springer Materials [30].

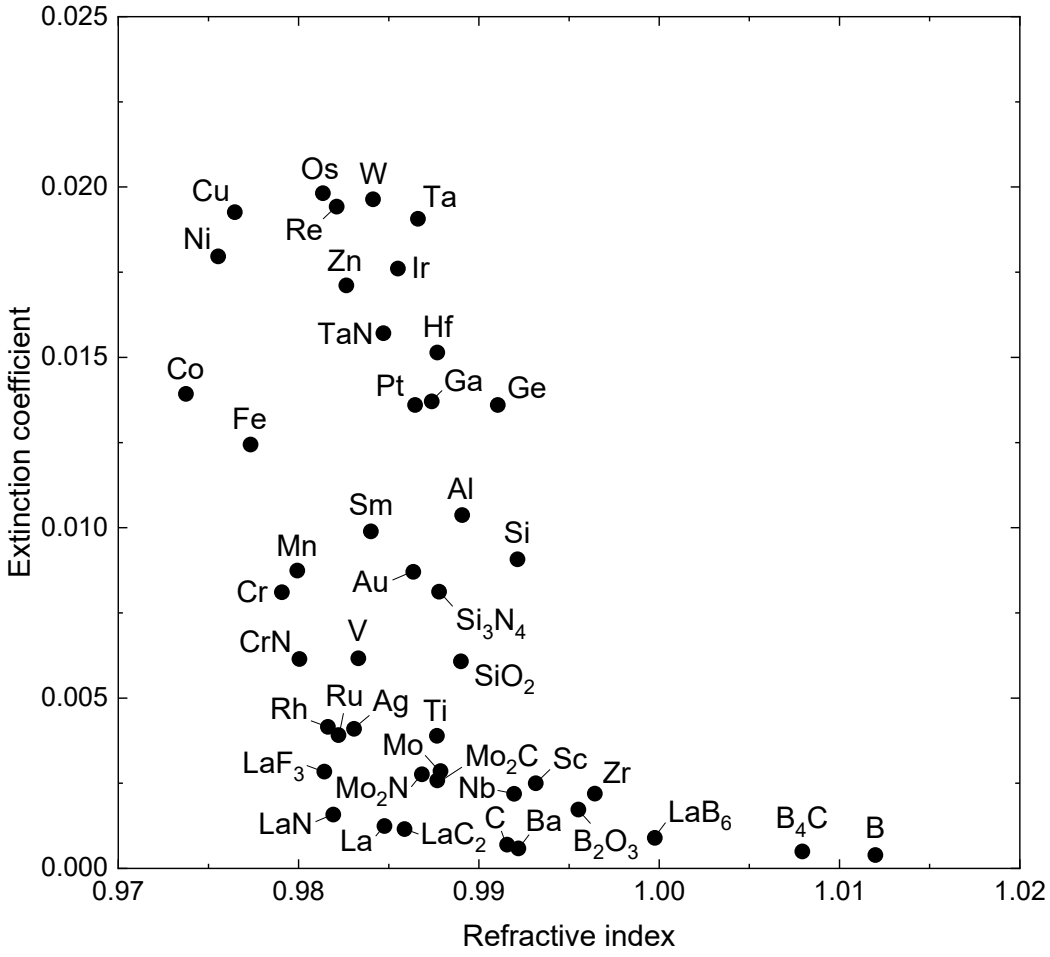

Fig. 5 Simulated optical constants at 6.60 nm wavelength.

(a)

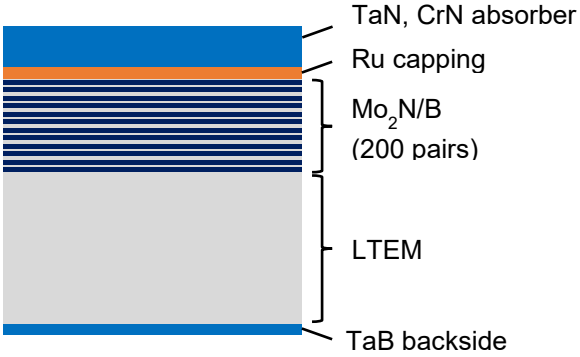

(b)

Material	Refractive index	Extinction coefficient
TaN	0.984706	0.015707
CrN	0.980045	0.006142
Ru	0.982217	0.003912
Mo_2N	0.986841	0.002761
B	1.011994	0.000388

Fig. 6 (a) Schematic of proposed BEUV mask blanks, (b) Simulated mask data at 6.60 nm wavelength.

3.2 Mask structure

We propose a BEUV mask blank as shown in Fig. 6-(a). The mask structure is composed of Mo_2N/B ML with 200 pairs, Ru capping layer, and absorber on a low thermal expansion substrate (LTEM) with TaB backside layer, assuming zero roughness at all interfaces. The Mo_2N/B ML is used as a BEUV mirror with an optimized thickness of 1.30 nm/2.00 nm at 6.60 nm wavelength with AOI of 6° [31]. The Ru capping thickness is 3.0 nm for repair durability while designing BEUV masks as well as EUV masks [32,33]. In this paper, we compare TaN with CrN as BEUV absorber candidates, and the optical constants of materials are shown in Fig. 6-(b) [29,30]. The TaB backside layer compensates for mask curvature and enables electrostatic chucking.

3.3 TaN and CrN absorbers

Figs. 7-(a) and (b) show the simulated reflectivity and phase difference based on the Parratt model, as the dependences of TaN and CrN absorber thickness at 6.6 nm wavelength and AOI of 6°. TaN provides a greater decrease in reflectivity than CrN, while CrN yields a greater phase shift for the same absorber thickness. At a phase difference of 135°, the thicknesses are 79.4 nm with 0.8 % for TaN and 62.6 nm with 17.1 % for CrN. TaN exhibits a significant decrease below 1 % at thicknesses above 70 nm, whereas CrN retains a reflectivity of 10.8 % at 83.0 nm thickness, and a phase difference of 180°. These results indicate that CrN is suitable for Att-PSMs because it provides sufficient margin against the reflectivity loss, and the sub-1 % reflectivity of TaN is usable for binary masks.

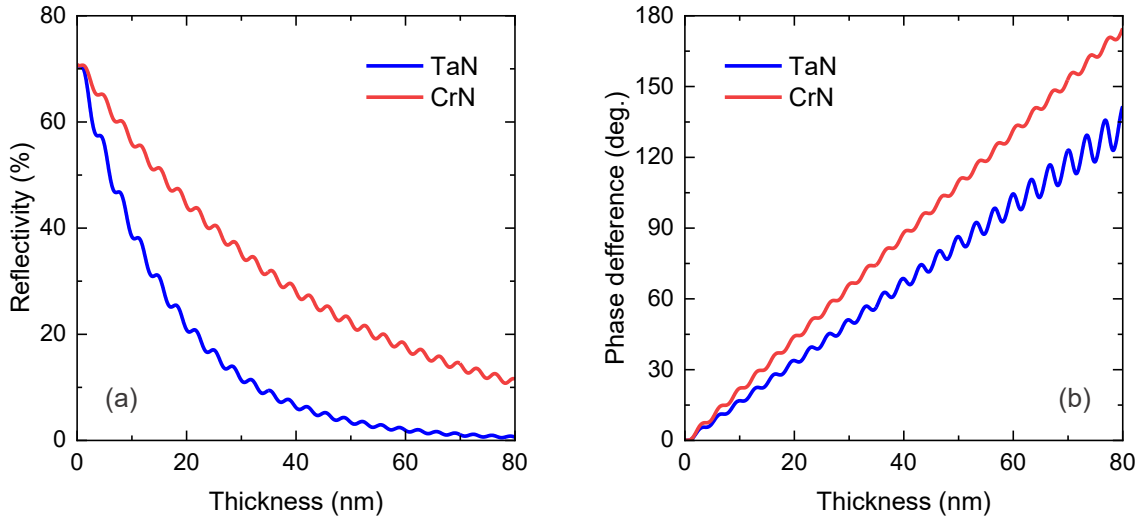

Fig. 7 (a) Simulated dependence of BEUV reflectivity on the absorber thickness, (b) Simulated dependence of phase difference on the absorber thickness.

The aerial image and the normalized image logarithmic slope (NILS) of the CrN-based Att-PSMs are formulated. Using the Abbe's method, each light source point $f_s \in [-\delta\,\mathrm{NA}/\lambda,\ +\delta\,\mathrm{NA}/\lambda]$, and the diffraction orders passing through the pupil ($|f_s + f_m| \le \mathrm{NA}/\lambda$, $f_m = m/P$) interfere coherently, and the partial image is summed incoherently in intensity over the source by Eq. (14).

$$I(x) = \frac{1}{N_s}\sum_{f_s}\left|\sum_{m:\ |f_s+f_m|\le \mathrm{NA}/\lambda} F_m\, e^{\,ik_0 W}\, e^{\,i2\pi f_m x}\right|^2 \tag{14}$$

The defocus z enters through the wavefront aberration in its exact, non-paraxial form $W = z(\cos\theta - 1)$, where $\sin\theta = \lambda(f_s + f_m)$. The complex reflectance of r_{abs} (absorber/line) and r_{ref} (space) with absorber thickness d_{abs} are obtained after phase correction as given by Eq. (15).

$$r^c_{\mathrm{abs}} = r_{\mathrm{abs}}\exp\left(-2i\,k_{z,\mathrm{vac}}\,d_{abs}\right), \qquad k_{z,\mathrm{vac}} = k_0\cos\theta_0 \tag{15}$$

The Fourier coefficients of a lattice $r(x)$ with period P and duty ratio d are given as Eq. (16).

$$F_0 = r^c_{\mathrm{abs}}\,d + r_{\mathrm{ref}}(1-d), \qquad F_{m\neq 0} = (r^c_{\mathrm{abs}} - r_{\mathrm{ref}})\frac{\sin(\pi m d)}{\pi m}\,e^{-i\pi m d} \tag{16}$$

The NILS is evaluated at the threshold $I_{\mathrm{th}} = (I_{\max} + I_{\min})/2$ and normalized by the line width ($w = P/2$ where P is the pitch), given as Eq. (17).

$$\mathrm{NILS} = w\left|\frac{d\ln I}{dx}\right| = \frac{P}{2}\left|\frac{1}{I}\frac{dI}{dx}\right| \tag{17}$$

A greater NILS denotes a sharper aerial image edge and larger exposure latitude at a given focus, and the NILS increases with higher NA.

Fig. 8-(a) shows the dependence of NILS on CrN thickness for 0.55 NA, 0.75 NA, and 0.85 NA. NILS rises with absorber thickness and saturates around 62.6 nm for the 0.55 NA, where CrN absorber gives a phase difference of 135°. The NILS values are 2.9 (0.55 NA), 4.2 (0.75 NA), and 4.6 (0.85 NA) when CrN absorber thickness is 80 nm. A higher NA gives a higher saturated NILS, and the relative gain from 0.55 NA to 0.85 NA is around 60 %. Fig. 8-(b) shows the aerial images for the three NAs when CrN = 62.6 nm. The DOF decreases with NA, the 0.55 NA remains broad and relatively flat across the entire scanned range, whereas the 0.85 NA curve forms a sharp peak.

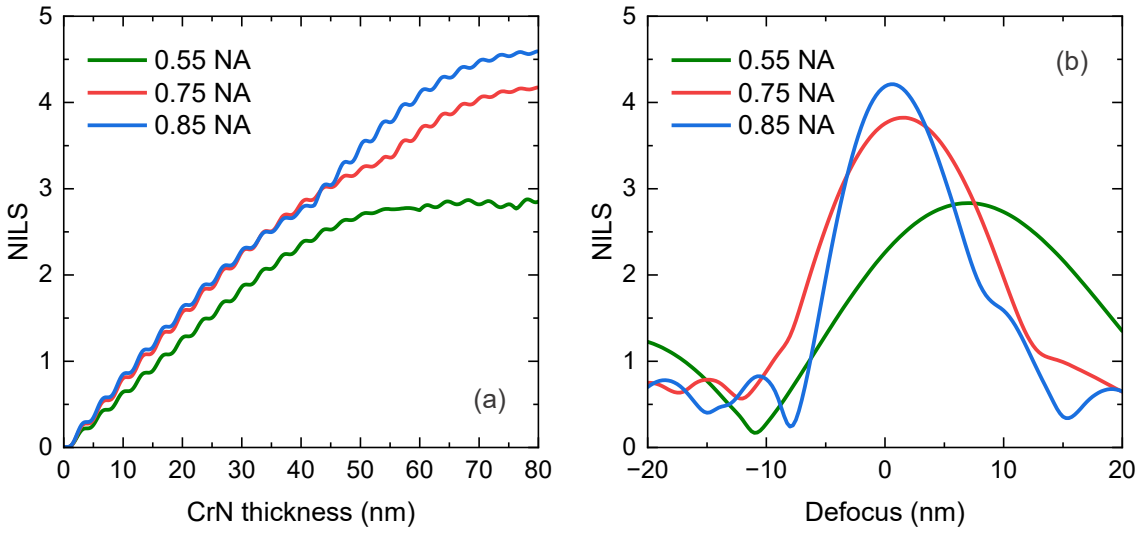

Fig. 8 (a) Simulated dependence of NILS on CrN thickness, (b) Simulated aerial images with CrN = 62.6 nm.

For M3D effect suppression, the sum of d_{abs} and Z_{eff} for a mask is required to be a smaller CD_{mask} on the mask as given by Eq. (18).

$$CD_{mask} = 2(d_{abs} + Z_{\text{eff}}) \tan\theta_i \tag{18}$$

Z_{eff} of Mo_2N/B ML is estimated from the AOI and the phase given by Eq. (19) [34].

$$\varphi \propto 2 \times Z_{\text{eff}} \times \frac{2\pi}{\lambda} \times (1 - \cos\theta_i) \cong Z_{\text{eff}} \times \frac{2\pi}{\lambda} \times {\theta_i}^2 \tag{19}$$

Fig. 9-(a) shows the simulated reflectivity at 6.6 nm in the Mo_2N/B thickness of 1.30 nm/2.00 nm, 1.10 nm/2.20 nm, 1.16 nm/2.15 nm optimized for AOI of 6°, 7°, and 8°. The AOI ranges of reflectivity over 70 % are 3.8°, 3.4°, 2.8°, respectively. Fig. 9-(b) shows the relationship between the Z_{eff} and AOI range calculated by the second polynomial approximation. The Z_{eff} in Mo_2N/B MLs are around 72 nm (1.30 nm/2.00 nm, 0-6°) and 77 nm (1.10 nm/2.20 nm, 0-7°), and 70 nm (1.16 nm/2.15 nm, 0-8°) which are 1.6 times larger than Mo/Si ML for EUV lithography [35].

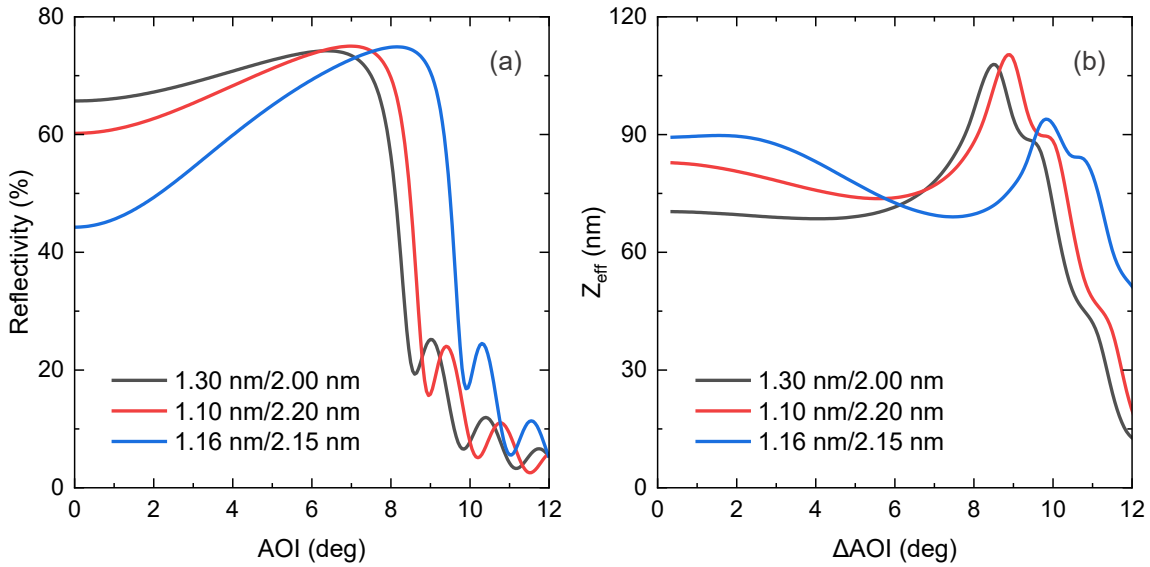

Fig. 9 (a) Simulated dependence of reflectivity at 6.60 nm on AOI in Mo_2N/B ML of 200 pairs, (b) The calculation of the Z_{eff} and the AOI range in Mo_2N/B ML of 200 pairs.

Table 2 summarizes the illumination-cone half-angles ($\alpha \parallel$, $\alpha \perp$) and common-plane phase variation ($\Delta\varphi_{cp} = \arg[R_{abs}/R_{ref}]$) for BEUV imaging with NA = 0.55, 0.75, and 0.85. We compare isomorphic 4x DM with anamorphic 4×/8× DM. At 0.55 NA, the anamorphic 4×/8× configuration keeps the chief-ray angle at object (CRAO) = 6° while halving the in-plane mask-side NA. For an anamorphic pupil, the cone half-angle is direction-dependent as $\alpha = \arcsin(NA/DM \parallel)$ in the plane of incidence $DM \parallel = 8$ and $\alpha = \arcsin(NA/DM \perp)$ in the cross-plane $DM \perp = 4$. At 0.55 NA, this reduces the in-plane full cone angle (2α) from 15.8° to 7.9° and the common-plane phase variation from 15.0° to 7.5°. The isomorphic 4x configuration at 0.55 NA is non-telecentric because $\alpha \parallel$ = 7.9° exceeds the 6° CRAO budget and causes incident/reflected pupil overlap. The 0.55 NA with 4×/8× DM and CrN of 62.6 nm is adopted as the high-NA BEUV architecture because the CD_{mask} for 0.75 NA and 0.85 NA are greater, assuming that CrN = 62.6 nm and Z_{eff} at AOIs in Fig. 9-(b).

Table. 2 Specification of BEUV mask and lithography.

NA	DM	$\alpha \parallel$ (deg)	$\alpha \perp$ (deg)	$\Delta\varphi_{cp}$ (deg)	AOI (deg)	CD_{mask} (nm)	CD_{wafer} (nm)
0.55	4x	7.9	7.9	15.0	≥ 7.9	≥ 36.8	≥ 9.2
	4x/8x	3.9	7.9	7.5	≥ 3.9	≥ 18.4	≥ 2.3, ≥ 4.6
0.75	4x/8x	5.4	10.8	8.0	≥ 5.4	≥ 25.4	≥ 3.2, ≥ 6.4
0.85	4x/8x	6.1	12.3	15.0	≥ 6.1	≥ 29.8	≥ 3.7, ≥ 7.5

3.4 *Black border*

We propose the BEUV black border (BB) shown in Fig. 10-(a), which suppresses BEUV and deep ultraviolet (DUV) reflectivity. BBs require BEUV reflectivity of less than 0.05 %, and DUV reflectivity of less than 1.0 % , over the wavelength range from 190 to 270 nm, outside the Lyman-Werner bands in the presence of a hydrogen background gas [36,37]. Fig. 10-(b) shows the optical constants of Ta, SiO_2, and Ta_2O_5 from 0.01 to 300 nm for calculating BB reflectivity [29,38].

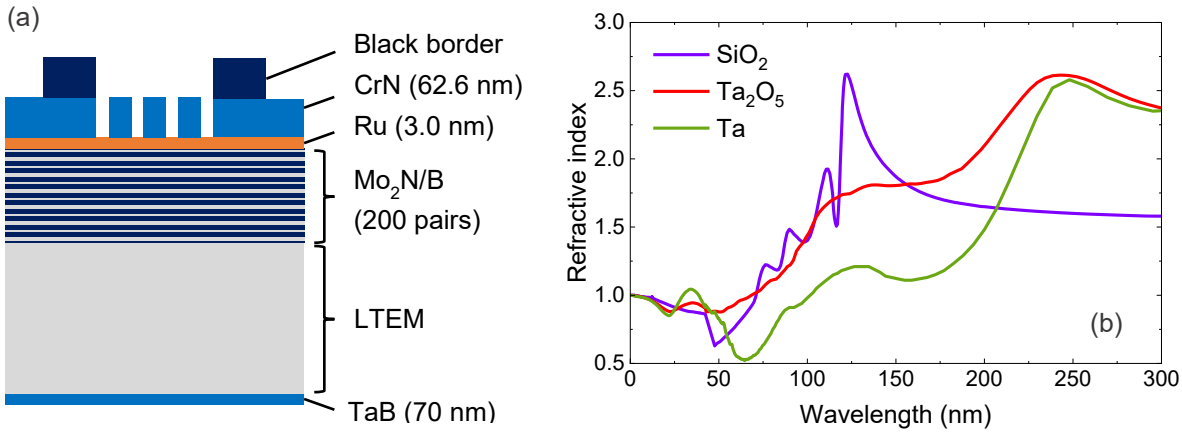

Fig. 10 (a) Schematic of proposed BBs on masks, (b) Optical constants from 0.01 to 300 nm.

The BB is composed of SiO_2 (top)/Ta_2O_5/Ta (bottom) as 17.1 nm/12.3 nm/166.3 nm. Figs. 11-(a) and (b) show that the BEUV reflectivity using the model of Fig. 10-(a), is less than 0.05 %, and the DUV reflectivity is below 1 % between 190 nm and 270 nm modeled as vacuum/BB/vacuum.

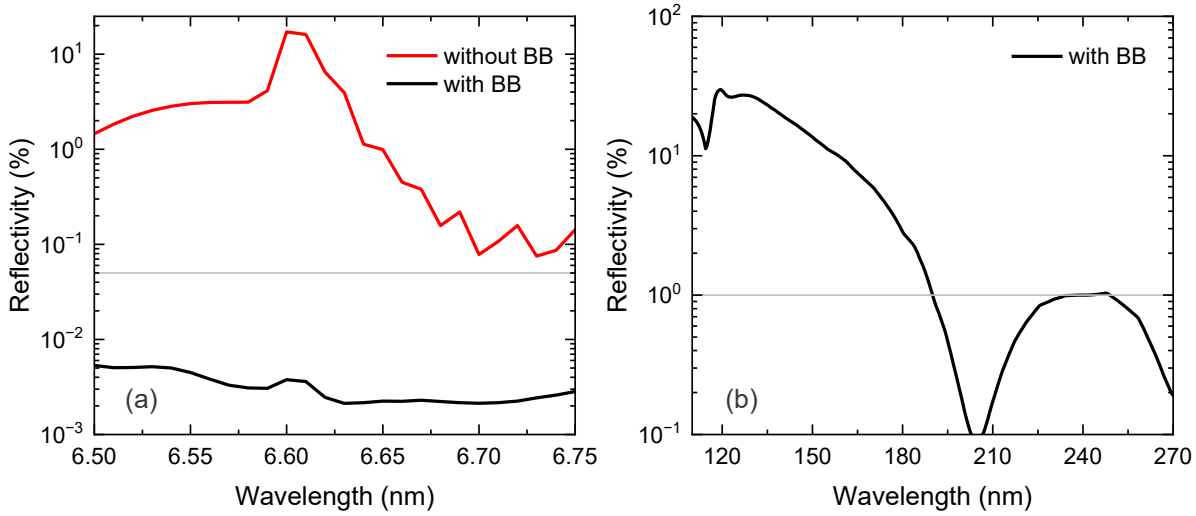

Fig. 11 Simulated reflectivity of SiO_2/Ta_2O_5/Ta BB for (a) BEUV and (b) DUV.

4 Conclusion

We propose a materials-kinetic rationale to suppress surface roughness using nitride-based components in BEUV mirrors and masks. Our model suggests a route for the suppression of kinetic roughness during thin film growth, assuming chemisorption coverage modifies the kinetic barriers for adatom diffusion and the ES reflection in the SOS model. For the BEUV photomask, we evaluate the Att-PSM architecture using Mo_2N/B ML, Ru capping, and CrN absorber. This model shows that 0.55 NA with 4x/8x DM at an AOI of 6° is promising for high-NA BEUV lithography.

Disclosures

The authors declare that there are no financial interests, commercial affiliations, or other potential conflicts of interest that could have influenced the objectivity of this research or the writing of this paper.

Code, Data, and Materials Availability

The data that supports the findings of this study are available from the corresponding authors on request and https://github.com/nhayase/JM3-260022P-1.

Acknowledgments

This work was partially supported by Hyogo Earthquake Memorial 21st Century Research Institute, Hyogo Foundation for Science and Technology, Tanaka Kikinzoku Memorial Foundation, and Takahashi Industrial and Economic Research Foundation.

References

1. N. Hayase, T. Harada, "Beyond EUV binary and phase shift masks simulation," *Proc. SPIE* **13177**, 315-322 (2024).
2. I. Lee, J. H. Franke, V. Philipsen, K. Ronse, S. De Gendt, E. Hendrickx, "Study on next-generation EUV lithography technology: hyper NA, the highest potential for practical implementation," *ACS Appl. Mater. Interfaces* **17**(33), 47719-47735 (2025).
3. T. Liang, H. Miyai, S. Sayan, M. Mizoguchi, K. Gondaira, M. Nishizawa, T. Suzuki, T. Todoroki, Y. Li, F. Abboud, "Actinic mask inspection for the era of high-numerical aperture extreme ultraviolet lithography," *J. Micro/Nanopatterning Mater. Metrol.* **24**(1), 011006 (2025).

4. Y. Chen, D. Hahner, M. Trubetskov, S. Schrameyer, W. Sakiew, K. Starke, V. Pervak, "Comparison of magnetron sputtering and ion beam sputtering on dispersive mirrors," *Appl. Phys. B* **126**(5), 82 (2020).
5. K. Rook, A. Checco, P. Turner, A. A. Kulkarni, K. Yamamoto, M. H. Lee, "Comparison of deposition techniques for Mo/Si reflective multilayers for EUV mask blanks," *Proc. SPIE* **11854**, 115-120 (2021).
6. S. Sherwin, M. Hettermann, D. Houser, P. Naulleau, "Understanding and measuring EUV mask 3D effects," *J. Micro/Nanopatterning Mater. Metrol.* **23**(4), 041407 (2024).
7. A. Erdmann, H. Mesilhy, P. Evanschitzky "Attenuated phase shift masks: a wild card resolution enhancement for extreme ultraviolet lithography?" *J. Micro/Nanopatterning Mater. Metrol.* **21**(2), 020901 (2022).
8. E. L. Church, P. Z. Takacs, "Handbook of Optics, Vol. 1, Chapter 7 Surface Scattering," *McGraw-Hill* (1995).
9. J. E. Harvey, S. Schröder, N. Choi, A. Duparré, "Total integrated scatter from surfaces with arbitrary roughness, correlation widths, and incident angles," *Opt. Eng.* **51**(1), 013402 (2012).
10. L. G. Parratt, "Surface studies of solids by total reflection of X-rays," *Phys. Rev.* **95**(2), 359 (1954).
11. D. K. G. De Boer, "X-ray reflection and transmission by rough surfaces," *Phys. Rev. B* **51**(8), 5297 (1995).
12. R. A. L. Almeida, S. O. Ferreira, T. J. Oliveira, F. A. Reis, "Universal fluctuations in the growth of semiconductor thin films," *Phys. Rev. B* **89**(4), 045309 (2014).
13. M. Kardar, G. Parisi, Y. C. Zhang, "Dynamic scaling of growing interfaces," *Phys. Rev. Lett.* **56**(9), 889 (1986).
14. Chi-Hang Lam, F. G. Shin, "Anomaly in numerical integrations of the Kardar-Parisi-Zhang equation," *Phys. Rev. E* **57**(6), 6506 (1998).
15. J. M. Kim, J. M. Kosterlitz, "Growth in a restricted solid-on-solid model," *Phys. Rev. Lett.* **62**, 2289 (1989).
16. M. Siegert, M. Plischke, "Solid-on-solid models of molecular-beam epitaxy," *Phys. Rev. E* **50**(2), 917 (1994).
17. G. Ehrlich, F. G. Hudda, "Atomic View of Surface Self-Diffusion: Tungsten on Tungsten," *J. Chem. Phys.* **44**, 1039–1049 (1966).
18. R. L. Schwoebel, E. J. Shipsey, "Step Motion on Crystal Surfaces," *J. Appl. Phys.* **37**(10), 3682–3686 (1966).
19. F. Family, T. Vicsek, "Scaling of the active zone in the Eden process on percolation networks and the ballistic deposition model," *J. Phys. A: Math. Gen.* **18** L75 (1985).

20. J. Krug, “Origins of scale invariance in growth processes,” *Adv. Phys.* **46**(2), 139–282 (1997).
21. S. F. Edwards, D. R. Wilkinson, “The Surface Statistics of a Granular Aggregate,” *Proc. R. Soc. Lond. A* **381**, 17 (1982).
22. O. A. Hougen, K. M. Watson, “General principles,” *Ind. Eng. Chem.* **35**(5), 529-541 (1943).
23. M. Copel, M. C. Reuter, E. Kaxiras, R. M. Tromp, "Surfactants in epitaxial growth," *Phys. Rev. Lett.* **63**, 632–635 (1989).
24. J. Villain, “Continuum models of crystal growth from atomic beams with and without desorption,” *J. Phys. I* **1**, 19–42 (1991).
25. W. W. Mullins, “Theory of Thermal Grooving,” *J. Appl. Phys.* **28**, 333–339 (1957).
26. R. M. Ziff, E. Gulari, Y. Barshad, "Kinetic phase transitions in an irreversible surface-reaction model," *Phys. Rev. Lett.* **56**(24), 2553–2556 (1986).
27. S. Berg, T. Nyberg, "Fundamental understanding and modeling of reactive sputtering processes," *Thin Solid Films* **476**(2), 215–230 (2005).
28. D. S. Sivia, “Elementary scattering theory: for X-ray and neutron users,” *Oxford University Press* (2011).
29. B. L. Henke, E. M. Gullikson, J. C. Davis, “X-ray interactions: photoabsorption, scattering, transmission, and reflection at E= 50-30,000 eV, Z= 1-92,” *Atomic data and nuclear data tables* **54**(2), 181-342 (1993).
30. Springer Materials, https://materials.springer.com
31. N. Hayase, M. Yoshimura, S. Suzuki, S. Yamakawa, T. Harada, “Mo-based multilayer for beyond EUV lithography,” *Proc. SPIE* **13983** (2026).
32. M. Singh, J. J. M. Braat, “Capping layers for extreme-ultraviolet multilayer interference coatings,” *Opt. Lett.* **26**(5), 259 (2001).
33. H. Over, Y. B. He, A. Farkas, G. Mellau, C. Korte, M. Knapp, M. Chandhok, M. Fang, “Long-term stability of Ru-based protection layers in extreme ultraviolet lithography: A surface science approach,” *J. Vac. Sci. Technol. B* **25**, 1123–1138 (2007).
34. M. F. Bal, M. Singh, J. J. M. Braat “Optimization of multilayer reflectors for extreme ultraviolet lithography,” *J. Micro/Nanolithogr., MEMS, MOEMS* **3**(4), 537-544 (2004).
35. O. Wood II, K. Wong, V. Parks, P. Kearney, J. Meyer-Ilse, V. Luong, V. Philipsen, M. Faheem, Y. Liang, A. Kumar, E. Chen, C. Bennett, B. Fu, M. Gribelyuk, W. Zhao, P. Mangat, P. Van der Heide, “Improved Ru/Si multilayer reflective coatings for advanced extreme-ultraviolet lithography photomasks,” *Proc. SPIE* **9776**, 364-373 (2016).
36. H. Abgrall, E. Roueff, F. Launay, J. Y. Roncin, J. L. Subtil, “The Lyman and Werner Band Systems of Molecular Hydrogen,” *J. Mol. Spectrosc.* **157**(2), 512-523 (1993).

37. M. A. van de Kerkhof, F. Liu, M. Meeuwissen, X. Zhang, M. Bayraktar, R. C. de Kruif, N. V. Davydova, "High-power EUV lithography: spectral purity and imaging performance," *J. Micro/Nanolithogr., MEMS, MOEMS* **19**(3) (2020).
38. L. V. Rodríguez-de Marcos, J. I. Larruquert, J. A. Méndez, J. A. Aznárez, "Self-consistent optical constants of SiO_2 and Ta_2O_5 films," *Opt. Mater. Express* **6**, 3622-3637 (2016).

Biographies and photographs for the other authors are not available.